Communication

Integration of Second-Order Bandstop Filter Into a Dual-Polarized 5G Millimeter-Wave Magneto-Electric Dipole Antenna

Jiangcheng Chen, Markus Berg, Kimmo Rasilainen, Zeeshan Siddiqui, Marko E. Leinonen, and Aarno Pärssinen

***Abstract*— This communication proposes a dual-wideband differentially fed dual-polarized magnetoelectric (ME) dipole with second-order bandstop filtering for millimeter-wave (mm-Wave) applications at 24.25–29.5 GHz and 37–43.5 GHz. Without disturbing the complementary antenna operation, two resonator types (hairpin and coupled $\lambda/4$ open-/short-circuited stub resonators) are embedded into the wideband ME dipole to create two transmission poles and two zeros for sharp band-edge selectivity. This allows independent manipulation of the transmission poles and zeros and a compact ME dipole size. The filtering antenna has more than 31.6 dB of port-to-port isolation. Measured results show symmetrical E- and H-plane radiation patterns and cross-polarization levels lower than −25.1 dB. The measured gains of the single element and a 2 × 2 array are 8.3 and 12.5 dBi, respectively. In addition, the band rejection reaches 23.7 and 21.8 dB for single element and array, respectively.**

***Index Terms*— Fifth generation (5G), band-notched antenna, complementary antenna, dual-band antenna, dual-polarized antenna, equivalent circuit model, filter, magnetoelectric (ME) dipole, millimeter-wave (mm-Wave).**

I. Introduction

Fifth-generation (5G) wireless communication uses millimeter-wave (mm-Wave) frequencies for high data rates, large channel capacity, and low latency [1]. Several mm-Wave bands at 24.25–29.5 and 37–43.5 GHz have been allocated for 5G systems as 5G New Radio FR2 bands n257–n261 [2]. Due to wide spectrum, broadband, dual-band, or multiband mm-Wave antennas [3], [4], [5] are needed to cover all the desired subbands with a simple feed solution for miniaturization, ease of integration with antenna-in-package (AiP) technology, and low fabrication cost. Dual-polarized operation with high cross-polarization discrimination (XPD) and port-to-port isolation is also needed to increase channel capacity and reduce multipath fading effects using polarization diversity [6], [7].

One solution is to cover the 5G FR2 lower band (LB) subbands at 24.25–29.5 GHz (19.5%) and upper band (UB) at 37–43.5 GHz (16.2%) by a broadband antenna operating from 24.25 to 43.5 GHz (56.8%). For broader bandwidths (BWs), one approach is to combine multimodes (e.g., higher order modes) by modifying the antenna structure while the lower modes remain stable, such as the circular patch [8] and E-shaped patch [9]. Another way is to stack multiple broadside radiators with a compact footprint [10]. These designs have insufficient bandwidth, and they are only single-polarized.

Alternatively, the 5G FR2 LB and UB can be covered using a dual-wideband antenna. At mm-Wave frequencies, quarter-mode substrate-integrated waveguide (SIW) antennas [11], [12], [13] have been used for dual-band operation with compact dimensions, low profile, and ease of integration. However, owing to single-SIW mode operation, they can only cover the single subband, i.e., 28-GHz (27.5–29.5 GHz) and 38-GHz (37–38.6 GHz) subbands at LB and UB, respectively. Another popular dual-band antenna is shared aperture antenna, such as an SIW slot array antenna [14], a microstrip grid antenna with parasitic patches [15], a differentially fed slot antenna loaded with a dielectric resonator antenna [16], and a combined-ridge-groove-cap-waveguide-fed shared circular aperture antenna [17]. Still, these works cannot cover the required LB and UB simultaneously, with a maximum bandwidth of 15.7% and 16.7% at their lower and upper operating bands, respectively. Other dual-band antenna types (e.g., metasurface-based dual-band antennas [3], [18], [19], gridded patch [20], scalable antenna [21], [22]) show sufficient bandwidth, but for only one band at a time (either LB or UB).

Filtering antennas can be implemented to replace the filter in RF frontend, which reduces the insertion loss (see, e.g., [23]). In [2], a U-shaped dipole with parasitic patch was proposed with bandstop filtering characteristic which can fully cover the 5G NR mm-wave bands of n257–n261. However, the XPD and isolation are both at a level of 20 dB, and the band-edge selectivity at the stopband is poor. The antenna in [22] also shows a bandstop response at the mid-band of LB and UB, but its rejection level is around 10 dB. This communication presents a dual-polarized differential probe-fed magnetoelectric (ME) dipole for 5G mm-Wave bands with simultaneous LB and UB operation. The proposed antenna combines a second-order bandstop filter with a recently reported complementary antenna [24] containing two electric dipole modes and one magnetic dipole mode. The antenna has high band-edge selectivity and controllable bandwidth at stopband, and its main novelties can be summarized as follows.

1) Two physically isolated resonators (hairpin and coupled stubs with different ground references) allow independent control of the location of the transmission zeros/poles, stopband edge selectivity, band-rejection level, and bandwidth of the stopband.
2) The coupled stub uses broadside coupling for structural symmetry. With high quality factor (Q) due to coupling between the open- and short-circuited stubs, it is possible to design a narrowband filter.
3) Nonredundant transmission lines connecting the upper layer hairpin resonators and lower layer stub resonators into the filter design make the bandstop filter quasi-optimal with steeper attenuation.

Manuscript received 30 October 2023; revised 3 April 2024; accepted 12 April 2024. Date of publication 7 May 2024; date of current version 7 June 2024. This work was supported in part by Nokia Corporation Ltd., in part by the Research Council of Finland through the 6G Flagship Program under Grant 346208, and in part by the Business Finland RF Sampo Project under Grant 2993/31/2021. The work of Jiangcheng Chen was supported in part by the Nokia Foundation, in part by the HPY Research Foundation, and in part by the Riitta and Jorma J. Takanen Foundation. *(Corresponding author: Jiangcheng Chen.)*

Jiangcheng Chen, Kimmo Rasilainen, Zeeshan Siddiqui, Marko E. Leinonen, and Aarno Pärssinen are with the Centre for Wireless Communications, University of Oulu, 90570 Oulu, Finland (e-mail: jiangcheng.chen@oulu.fi).

Markus Berg is with ExcellAnt Ltd., 90590 Oulu, Finland.

Color versions of one or more figures in this article are available at https://doi.org/10.1109/TAP.2024.3395990.

Digital Object Identifier 10.1109/TAP.2024.3395990

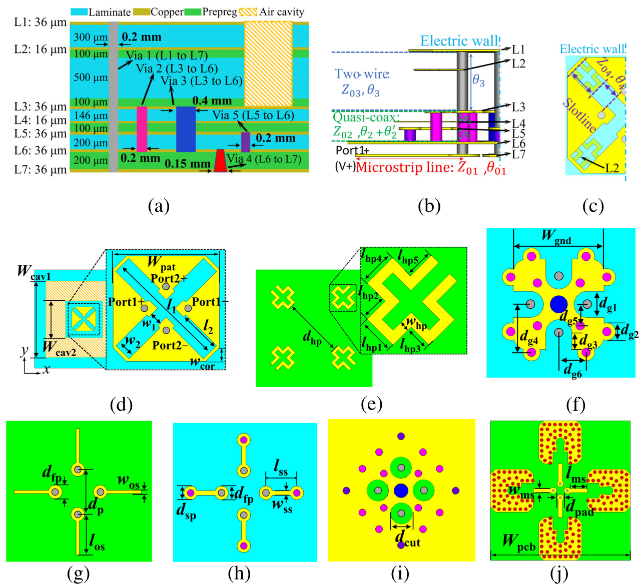

Fig. 1. Proposed filtering antenna geometry. (a) PCB stack. (b) Side view. (c) Top view. (d)–(j) Description of metal layers L1–L7.

TABLE I

DIMENSIONS (IN mm) OF THE SECOND-ORDER FILTERING ANTENNA

Param.	W_{pat}	W_{gnd}	W_{cav1}	W_{cav2}	W_{pcb}	W_{array}	w_{cor}
Value	3.15	2.08	10	5	13	35	0.4
Param.	w_1	w_2	w_{ms}	w_{hp}	w_{os}	w_{ss}	d_{pad}
Value	0.37	0.55	0.39	0.1	0.1	0.1	0.61
Param.	d_{g1}	d_{g2}	d_{g3}	d_{g4}	d_{g5}	d_{g6}	d_{cut}
Value	0.2	0.6	0.4	0.39	1.1	0.49	0.6
Param.	d_{hp}	d_{p}	d_{fp}	d_{sp}	l_{os}	l_{ss}	l_{ms}
Value	2.11	1.3	0.4	0.4	1.185	0.905	1.61
Param.	l_1	l_2	l_{hp1}	l_{hp2}	l_{hp3}	l_{hp4}	l_{hp5}
Value	3.69	1.3	0.35	0.245	0.245	0.345	0.28

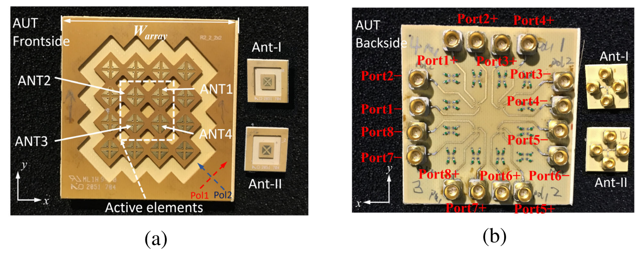

Fig. 2. Prototype of the fabricated 2 × 2 array and unit cells. (a) Top view. (b) Bottom view.

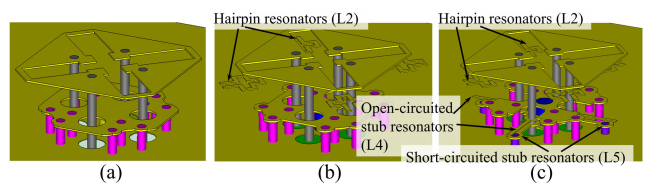

Fig. 3. Filtering antenna evolution. (a) Reference wideband (WB) antenna [24]. (b) First-order filtering (Ant-I). (c) Second-order filtering (Ant-II, proposed).

4) Adding the two resonator sets improves the matching while not breaking the ME dipole antenna operation nor increasing its footprint.

II. ANTENNA DESIGN

A. Unit Cell

Fig. 1 shows the printed circuit board (PCB) stack and layered view of the proposed differentially driven dual-wideband dual-polarized ME dipole antenna, which consists of a cross-slotted octagonal radiation patch (L1), four squeezed hairpin resonators (L2), an additional lifted ground (L3), four coupled $\lambda/4$ open-/short-circuited stub resonators (L4 and L5), a main ground (L6), and microstrip feedlines (L7). Panasonic Megtron 7 laminate and prepreg (bonding material) with $\varepsilon_{\text{r}} = 3.34$ and $\tan\delta = 0.003$ are used for the stack. Layers L1, L3, and L6–L7 are the same as in the reference wideband ME dipole antenna of [24], from which additional information on these layers can be found. Multilayer PCBs increase cost and complexity, but this can be a useful performance tradeoff in AiPs [22].

Four plated through-vias (Via 1) act as the feed probes (connecting the slotted patch on L1 to the microstrip feedlines on L7), and they are grouped in two differential pairs at opposite sides. Each differential pair can excite three desired complementary antenna modes for wideband operation. Quasi-coaxial shorting vias (Vias 2 and 3) encircle the feeding pins to eliminate the parallel-plate mode and to implement the vertical transition. Surface wave modes are suppressed with a 1-mm deep air cavity [25] around the antenna unit cell (UC).

To create transmission zeros between LB and UB, two resonator types are added to the reference design. Four hairpin resonators symmetrically below the slot along the E- and H-planes couple magnetically to the slot ends. With four $\lambda/4$ coupled open-/short-circuited stub resonators, one end of both the stubs connects directly to the feed probes (within the quasi-coaxial line), and a shorting via (Via 5) terminates the other end of the short-circuited stub to the main ground (L6).

Fig. 1(e) shows that the hairpin resonators are squeezed to miniaturize the $\lambda/2$ resonator and reduce its footprint. The open-circuited stubs of L4 and short-circuited stubs of L5 are broadside-coupled for high Q, using an embedded microstrip structure as shown in Fig. 1(g)–(h). The footprints of both the resonator types overlap under the patch for almost the same element size as without the resonators to miniaturize the design. Table I lists the optimized design parameters.

B. 2 × 2 Array

To verify the array performance of the proposed unit cell, a planar 2 × 2 array with ±45° slanted polarization is built (see Fig. 2). Four active elements in the middle of array are fed with individual differential pairs instead of a corporate feed network to see the isolation between adjacent and diagonal elements. The unit cell spacing is 0.57 λ_0 at 32 GHz (tradeoff between LB and UB operations).

The array has 12 dummy elements terminated to 50 Ω around the inner four active elements to overcome the edge effects [26] of the 2 × 2 array on a large ground plane. The air cavity around the dummy elements and between active elements reduces the substrate mode effect. Fig. 2(b) shows the rotationally symmetric feed network routing for four differential-fed dual-polarized active elements.

III. OPERATION PRINCIPLE

A. Evolution of the Second-Order Bandstop Antenna

To understand the operating principle of the proposed second-order bandstop antenna from the reference wideband ME dipole [24], Fig. 3 presents the antenna evolution step by step, and Fig. 4 shows the input impedance and reflection coefficient. The first modification (Ant-I) adds a set of hairpin resonators to create the first transmission zero. A second modification (Ant-II) adds coupled stub resonators to create a second transmission zero, to improve stopband rejection and band-edge selectivity, and to control the stopband BW. The coupled

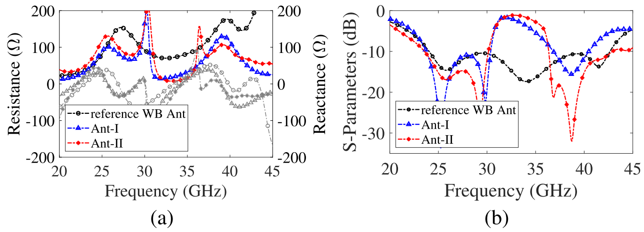

Fig. 4. (a) Input impedance and (b) reflection coefficients of the proposed second-order band-notched antenna (Ant-II) with comparison to reference wideband antenna and the first-order band-notched antenna (Ant-I).

stubs also create passband transmission poles whose locations can be controlled to enhance UB matching. As seen in Fig. 4(a), the differential input resistance of the reference wideband antenna varies around 100 Ω. The −10-dB bandwidth is 24.0–42.6 GHz which does not cover the desired n259 band (up to 43.5 GHz). After adding the hairpin resonators, the resistance is close to zero around 32 GHz, creating the first transmission zero (radiation null). The UB matching deteriorates, reaching only up to 40.5 GHz despite good LB matching. In addition, the upper stopband-edge selectivity is low.

Coupled $\lambda/4$ open-/short-circuited stub resonators are used as the second resonator type in Ant-II. They have high Q, compact size, and independent control of the transmission zeros and poles [27]. Traditional $\lambda/4$ open-/short-circuited stub resonators of [28] have low inductance and low Q, which is not suitable for narrowband bandstop filters. In [27], the open- and short-circuited stubs are folded to couple them to each other. This increases inductance, reduces the form factor, and increases Q. Transmission zeros and poles depend on the electrical length of open- and short-circuited stubs, respectively. Varying the length of short-circuited stub with fixed length of open-circuited stub causes different frequency shift at the upper and lower transmission poles for an extra degree of freedom in passband matching. However, the co-planar layout of the coupled stub resonators is asymmetric over the patch symmetry plane due to edge-coupling, which degrades port-to-port isolation and reduces XPD. PCB fabrication rules limit the possible line spacing and width, which can complicate designing narrow stubs and narrowband filters.

For structural symmetry, a symmetric broadside-coupled stub structure is used with the open- and short-circuited stubs at two successive layers (L4 and L5), as shown in Fig. 1(e)–(f). Coupling between two stub types can be altered by changing the laminate thickness between the layers. After adding the stub resonators, the resistance of Ant-II has a second transmission zero (radiation null) near 35 GHz. The UB bandwidth improves to cover the desired bands, while both the LB matching and the first transmission zero remain stable (see Fig. 4). This improves the upper band-edge selectivity at stopband. In addition, the location of the second resonator below the lifted ground has low coupling to the hairpin resonators due to increased physical separation and different ground references to keep them working independently.

B. Filter Synthesis and Equivalent Circuit Model

Fig. 1(b) and (c) shows that each part of the feeding structure can be modeled as transmission line sections. From the differential port to the patch, the input signal sees a section of microstrip, quasi-coaxial, two-wire, and slotline transmission lines. Their characteristic impedances and electrical lengths are given in the original equivalent circuit model (ECM) of Fig. 5(a). The inset shows the schematic of the coupled open-/short-circuited stub. Since the used $\lambda/4$ coupled open-/short-circuited stub resonator acts as a series LC resonator at the center frequency [27], an open stub is used for convenience in the ECM. The $\lambda/2$ hairpin resonator is modeled as a short-circuited stub in series [29]. Z_A is the terminating impedance (the input impedance of the reference ME dipole). A circuit model for Z_A with three parallel-coupled serial RLC resonators is shown in [24].

Due to odd-mode excitation of a symmetrical network and the fact that a symmetry plane accounts for a short-circuit of the bisection (electric wall), the original equivalent circuit is developed into a simpler one in Fig. 5(b) in accordance with [24], [30]. Characteristic impedance values are halved as described in Fig. 5(b). Applying Kuroda's identities gives the resultant equivalent circuit of Fig. 5(c), corresponding to a typical second-order (two-pole) bandstop filter. The shunt $\lambda/4$ open-circuited stubs connect to unit elements whose lengths are $\lambda/4$ at the stopband center frequency in a traditional bandstop filter with open-circuited stubs. Hence, the connecting lines (θ_2', θ_3, and θ_4) between two stubs can be modeled as filter unit cells.

For better band-edge attenuation, the unit cell is made nonredundant to effectively make it an open-circuited stub [29], differing from the redundant one in a traditional bandstop filter. This makes the feeding probes in the proposed antenna part of the filter element. In narrowband filters, the stubs in a redundant design can become very narrow and hard to implement. Fabrication limits are more relaxed for a nonredundant design. Fewer stubs can produce a steeper stopband edge in a nonredundant unit cell than in a redundant one. A nonredundant design can be achieved by adjusting design parameters (e.g., terminating impedance, electrical length, and line impedance) of both the resonators and connecting lines shown in Fig. 5(c).

IV. Simulation and Measurement Results

The single element and 2 × 2 array of Fig. 2 are fabricated. The S-parameters of the antenna ports are measured using a Keysight N5247B PNA-X network analyzer. Radiation patterns of single and array elements are measured using the approach of [24].

A. Single Element

The simulated and measured S-parameters for Ant-I and Ant-II (single element) are presented in Fig. 6, with a decent agreement between the results. In simulations [Fig. 6(a)], Ant-I covers full LB for 5G n257, n258, and n261 bands (24.25–29.5 GHz) while it provides partial UB coverage (n260, 37–40 GHz only) with a slight UB resonance offset in the measurements. Ant-II obtains a −10-dB matching level across the desired LB and UB range, covering an overlapped bandwidth of 23.9–31.6 GHz (27.7%) at LB and 36.7–45.0 GHz (>20.3% as frequencies above 45 GHz were not studied) at UB for two orthogonal polarizations. The second transmission zero of Ant-II enhances selectivity at the upper bound of the stopband, which is also seen in the radiation efficiency of Ant-II compared with Ant-I in Fig. 7. The Ant-I/Ant-II achieves better than 40.2 dB/36.4 dB and 37.3 dB/31.6 dB of isolation at LB and HB, respectively. To verify the proposed ECM in Fig. 5(b), the analytical result is calculated and presented in Fig. 6(b), which agrees well with the numerical result.

Fig. 7 shows that Ant-I has a rather narrow stopband and limited band rejection (>19%). Adding coupled-stub resonators widens the stopband and brings the suppression below 10%. Filtering antenna selectivity is evaluated with the radiation suppression index (RSI) using 80% and 16% efficiency bandwidths [31]. Due to the dual nature of bandpass and bandstop filters, the inverse of the previous RSI is used for the proposed bandstop antenna. The calculated RSI values are 0.48 and 0.61 for single element and array, respectively.

The simulated and measured E- and H-plane radiation patterns are depicted in Fig. 8. As in [24], the azimuth plane measurement was limited to ±130° due to mechanical limitations of the used hardware, which also allowed pattern measurements only up to 40 GHz. The

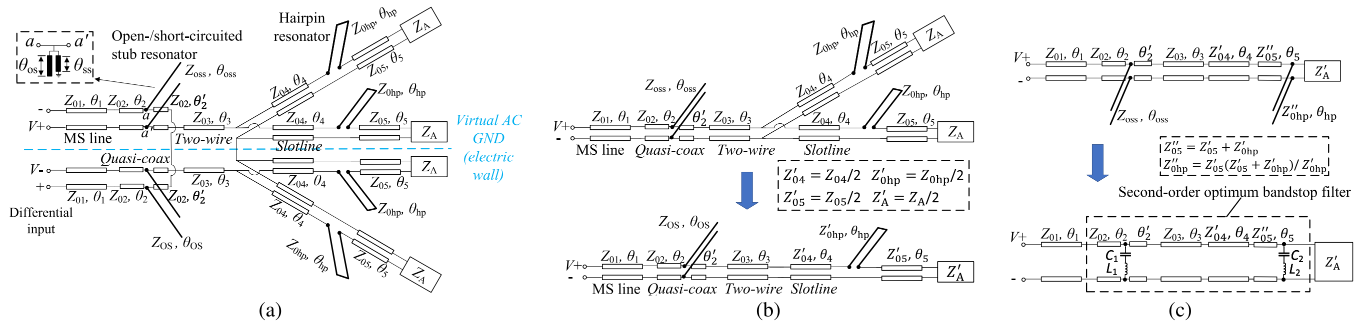

Fig. 5. Equivalent circuit model for the proposed filtering antenna. (a) Original circuit. (b) Simplified circuit (bisection). (c) Resultant equivalent circuit for the second-order optimum bandstop filter after applying Kuroda's identities. The circuit model is used to qualitatively explain the antenna operation.

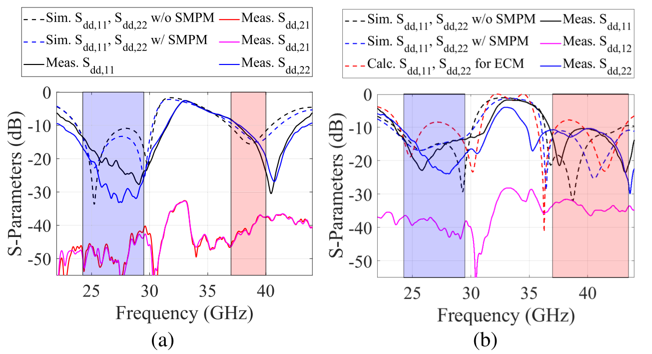

Fig. 6. *S*-parameters (sim. and meas.) of a single-element filtering antenna. (a) First-order bandstop filtering. (b) Second-order bandstop filtering.

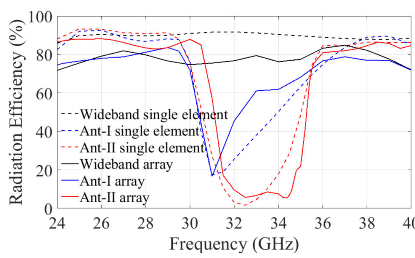

Fig. 7. Radiation efficiency of wideband, first-, and second-order filtering antennas.

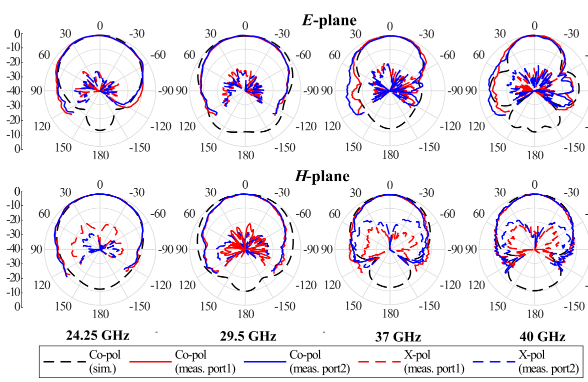

Fig. 8. Simulated and measured single-element radiation patterns with second-order filtering at 24.25, 29.5, 37, and 40 GHz.

simulated and measured co-polar patterns agree well, but the measured cross-polar level is more noticeable. This may result from slight asymmetry related to fabrication tolerances, or be caused by feed imbalance from coaxial cable and measurement inaccuracies (e.g., AUT alignment). The radiation patterns are stable and symmetric across a wideband at both LB and UB between two principle planes due to the ME dipole operation. Both the simulated and measured

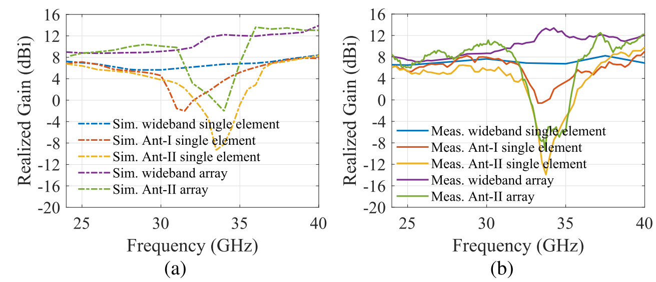

Fig. 9. Comparison of (a) simulated and (b) measured realized gains of wideband antenna and first- and second-order bandstop filtering antennas. (a) Simulation. (b) Measurement.

XPD levels are high at boresight as expected due to the symmetric structure, with the measured XPD of 27.4 and 25.1 dB across the frequencies of interest at LB and UB, respectively.

Fig. 9 shows that the simulated and measured realized gains of Ant-I and Ant-II agree well across the respective operation bands. At LB and UB, the measured gains of Ant-II are 4.8–6.4 and 6.1–9.8 dBi respectively. Dissipation effects in the bandstop filter slightly reduce the LB gain of the proposed bandstop antenna compared with the reference antenna: a finite Q (due to dielectric and metallic losses) causes some insertion loss in the resonators [29]. In contrast to the measured passband peak gain, Ant-I has only 9.6 dB of out-of-band rejection level while Ant-II gives 23.7 dB of rejection at stopband. The upper stopband edge of Ant-II is much sharper than that of Ant-I.

B. Parametric Study

1) Length and Location of the Hairpin Resonator: Fig. 10(a) shows that only the lower stopband edge shifts as the hairpin resonator length changes. A longer resonator moves the first transmission zero (around 32 GHz) generated by the hairpin resonator to lower frequency while the stopband upper bound remains fixed. The band-rejection level at stopband improves when the two transmission zeros get closer. In addition, the slope of the lower stopband edge stays the same while shifting with the resonator length.

Typically, the unit elements are redundant in traditional filter synthesis. Their filtering property is not used and they do not affect the filter selectivity [29]. In this work, the roll-off rate at stopband edges of the proposed antenna varies with the separation distance between two resonator types when modifying the location of the hairpin resonator presented in Fig. 10(b). Especially when increasing d_{hp} (θ_4), the lower stopband edge becomes steeper and the band-rejection level remains similar. This is because adjusting θ_4 changes the connecting line impedance Z'_{04} and Z''_{05}. In addition, the resonator location offset changes the ratio of coupled magnetic energy to the average stored energy which determines the overall

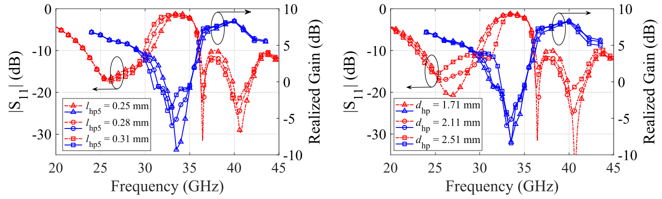

(a) (b)

Fig. 10. Effect of the hairpin resonator on filtering. (a) Resonator length. (b) Resonator location.

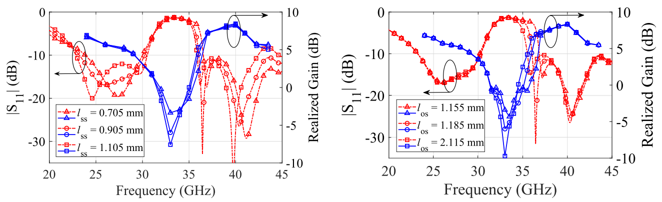

(a) (b)

Fig. 11. Effect of short- and open-circuited stub length on filtering. (a) Short-circuited stub length. (b) Open-circuited stub length.

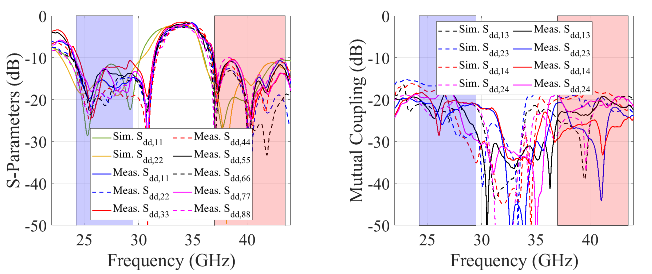

(a) (b)

Fig. 12. Simulated and measured *S*-parameters of the array elements. (a) Reflection coefficients. (b) Coupling between adj. elements.

Q, and hence the stopband BW varies. In short, the connecting transmission line impacts on the bandwidth and improves band-edge selectivity of the stopband, proving that the lines between the hairpin and coupled stub resonators are nonredundant unit cells. Thus, the proposed antenna operates as a quasi-optimum bandstop filter.

2) Length of the Open- and Short-Circuited Stubs: Fig. 11(a) shows that the LB and UB matching of the proposed antenna varies with the length of the short-circuited stub l_{ss}. As mentioned in Section III-A, the transmission zero and pole locations depend on the length of open-circuited l_{os} (or θ_{os}) and short-circuited stub l_{ss} (or θ_{ss}), respectively. With fixed l_{os}, shorter l_{ss} shifts the LB and UB transmission poles to higher frequencies at different rates with fixed transmission zeros created by the two sets of resonators.

In Fig. 11(b), increasing the length of open-circuited stub l_{os} (or θ_{os}) shifts the upper stopband edge to lower frequency while the lower band edge remains unchanged. Hence, the length of open-circuited stub only affects the location of the second transmission zero (around 35 GHz). In turn, the length of short-circuited stub mainly affects the location of transmission poles and the respective matching level at the left and right sides of the transmission zero. Varying the stub length maintains the slope of the upper stopband edge.

C. 2 × 2 Array

Fig. 12 gives the simulated and measured *S*-parameters of each unit cell antenna in the 2 × 2 array. All the active elements can cover the desired LB and UB for both the polarizations, except for slight deterioration for differential port 3 at the lower edge of LB. This effect can come from fabrication and assembly tolerances, or amplitude/phase imbalances in the feed cables. The simulated and measured mutual coupling levels generally agree well, and adjacent elements have higher coupling than diagonal ones across the whole band. For brevity, only the worst case (isolation between adjacent elements) is shown in Fig. 12(b). Isolation remains better than 15.9 dB within the LB and UB.

The simulated and measured radiation patterns for the array of Ant-II of Fig. 13 agree well. As the two polarizations have perfect symmetry, only one set of the patterns is provided. At the E- and H-planes, the XPD level is better than 22.8 dB at LB and 18.7 dB at UB, which are good levels for practical applications. The simulated and measured array gains are illustrated in Fig. 9. At LB and UB, the measured value is 6.1–11.1 and 8.9–12.5 dBi, respectively. The Ant-II array shows 15.5-dB suppression level while the second-order one provides 21.8-dB rejection at stopband. Gain enhancement for the array over a single element is lower at LB than at UB, probably due to stronger LB mutual coupling (see Fig. 12). This couples more power to other (dummy and active) elements and increases the LB radiation loss [24], [32]. Compared with simulations, the slight gain variation, beam tilt, and reduced XPD in the measured patterns relate to measurement and fabrication inaccuracies. The measured sidelobe level at both the planes is below −14.3 dB across the whole band. The calculated aperture efficiency for the proposed 2 × 2 array is 18.1% and 14.1% (including area of dummy elements), or 81.9% and 64% (without area of dummy elements), at LB and UB, respectively.

Table II shows comparison of the proposed dual-wideband dual-polarized antenna with the state of the art. Most reported works lack simultaneous LB and UB coverage (except [2]). The proposed complementary antenna is more broadband at both LB and UB, especially at UB due to the upper transmission pole from the coupled open/short-circuited stub resonator. Hence, the proposed antenna can cover 5G bands n257, n258, and n261 (24.25–29.5 GHz), and n259

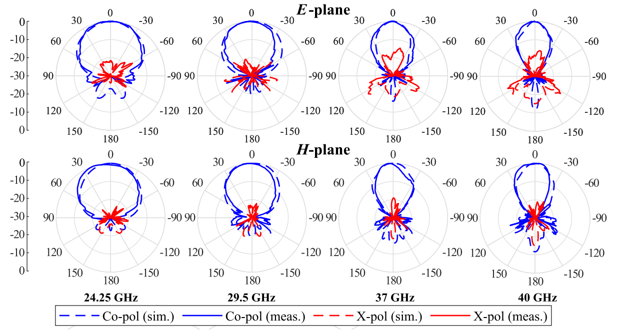

Fig. 13. Simulated and measured radiation patterns of the 2 × 2 array with second-order filtering at 24.25, 29.5, 37, and 40 GHz.

TABLE II

COMPARISON BETWEEN THE PROPOSED ANTENNA AND STATE-OF-THE-ART MM-WAVE ANTENNA DESIGNS

Ref.	Oper. band (GHz)	–10-dB BW (%)	Isol. (dB)	RSI (UC/Array)	G_{max} (dBi) (UC/Array)
[2]	24.0–30.0 37.0–43.5	22.2% 16.1%	>20 >20	N/A	–/7.1 –/8.2
[3]	23.7–29.2 36.7–41.1	20.7% 11.3%	N/A	N/A	7.2/– 10.9/–
[12]	26.7–30.4 36.6–38.8	12.8% 5.8%	N/A	N/A	–/10.1 –/10.2
[19]	23.8–27.7 36.8–44.4	15.2% 18.7%	35 28	N/A	7.7/11.0 13.0/15.5
[20]	23.3–31.7 42.5–46.5	30.5% 9.0%	17.1 18.3	N/A	–/14.8 –/14.1
[22]	24.25–29.5 37.0–40.0	19.5% 7.8%	20 20	0.43/–	3.5/7.0 4.5/10.0
This work	23.9–31.6 36.7–45.0	27.7% >20.3%	36.4 31.6	0.48/0.61	6.7/11.1 8.3/12.5

and n260 (37–43.5 GHz). It has a small size and much higher port-to-port isolation and XPD than most of the other reported designs.

V. Conclusion

A dual-wideband differentially fed dual-polarized ME dipole with second-order bandstop filtering operation for Ka-band applications is presented. The proposed antenna covers 5G bands n257, n258, and n261 (24.25–29.5 GHz), and n259 and n260 (37–43.5 GHz). Independently controlled transmission zeros and poles give sharp selectivity with RSI of 0.48 and 0.61 for element and array, respectively, and allow tuning the stopband BW and rejection level. The design keeps a compact footprint and has high port-to-port isolation of 36.4 and 31.6 dB and XPD of 27.4 and 25.1 dB at LB and UB, respectively. The rejection level for the proposed single element is as high as 23.7 dB. With good out-of-band rejection, compact size, simple,structure and low-cost fabrication, the proposed ME dipole is a promising candidate for mm-Wave AiP applications.

Acknowledgment

The authors would like to thank Mr. Markku Jokinen for help in the radiation pattern measurements. Keysight Inc. has supported the research by donating measurement equipment.

References

[1] T. S. Rappaport, Y. Xing, G. R. MacCartney, A. F. Molisch, E. Mellios, and J. Zhang, "Overview of millimeter wave communications for fifth-generation (5G) wireless networks-with a focus on propagation models," *IEEE Trans. Antennas Propag.*, vol. 65, no. 12, pp. 6213–6230, Dec. 2017.

[2] S. J. Yang, S. F. Yao, R.-Y. Ma, and X. Y. Zhang, "Low-profile dual-wideband dual-polarized antenna for 5G millimeter-wave communications," *IEEE Antennas Wireless Propag. Lett.*, vol. 21, no. 12, pp. 2367–2371, Dec. 2022.

[3] T. Li and Z. N. Chen, "A dual-band metasurface antenna using characteristic mode analysis," *IEEE Trans. Antennas Propag.*, vol. 66, no. 10, pp. 5620–5624, Oct. 2018.

[4] Y. Zhang and J. Mao, "An overview of the development of antenna-in-package technology for highly integrated wireless devices," *Proc. IEEE*, vol. 107, no. 11, pp. 2265–2280, Nov. 2019.

[5] K. Kibaroglu, M. Sayginer, and G. M. Rebeiz, "A low-cost scalable 32-element 28-GHz phased array transceiver for 5G communication links based on a 2 × 2 beamformer flip-chip unit cell," *IEEE J. Solid-State Circuits*, vol. 53, no. 5, pp. 1260–1274, May 2018.

[6] Q. Xue, S. W. Liao, and J. H. Xu, "A differentially-driven dual-polarized magneto-electric dipole antenna," *IEEE Trans. Antennas Propag.*, vol. 61, no. 1, pp. 425–430, Jan. 2013.

[7] R. Lian, Z. Wang, Y. Yin, J. Wu, and X. Song, "Design of a low-profile dual-polarized stepped slot antenna array for base station," *IEEE Antennas Wireless Propag. Lett.*, vol. 15, pp. 362–365, 2016.

[8] K. Zhang, Z. H. Jiang, W. Hong, and D. H. Werner, "A low-profile and wideband triple-mode antenna for wireless body area network concurrent on-/off-body communications," *IEEE Trans. Antennas Propag.*, vol. 68, no. 3, pp. 1982–1994, Mar. 2020.

[9] J. Yin, Q. Wu, C. Yu, H. Wang, and W. Hong, "Broadband symmetrical E-shaped patch antenna with multimode resonance for 5G millimeter-wave applications," *IEEE Trans. Antennas Propag.*, vol. 67, no. 7, pp. 4474–4483, Jul. 2019.

[10] P. A. Dzagbletey and Y.-B. Jung, "Stacked microstrip linear array for millimeter-wave 5G baseband communication," *IEEE Antennas Wireless Propag. Lett.*, vol. 17, pp. 780–783, 2018.

[11] T. Hong, Z. Zhao, W. Jiang, S. Xia, Y. Liu, and S. Gong, "Dual-band SIW cavity-backed slot array using TM020 and TM120 modes for 5G applications," *IEEE Trans. Antennas Propag.*, vol. 67, no. 5, pp. 3490–3495, May 2019.

[12] T. Deckmyn, M. Cauwe, D. V. Ginste, H. Rogier, and S. Agneessens, "Dual-band (28,38) GHz coupled quarter-mode substrate-integrated waveguide antenna array for next-generation wireless systems," *IEEE Trans. Antennas Propag.*, vol. 67, no. 4, pp. 2405–2412, Apr. 2019.

[13] Y.-X. Sun, D. Wu, X. S. Fang, and N. Yang, "Compact quarter-mode substrate-integrated waveguide dual-frequency millimeter-wave antenna array for 5G applications," *IEEE Antennas Wireless Propag. Lett.*, vol. 19, pp. 1405–1409, 2020.

[14] J. F. Zhang, Y. J. Cheng, Y. R. Ding, and C. X. Bai, "A dual-band shared-aperture antenna with large frequency ratio, high aperture reuse efficiency, and high channel isolation," *IEEE Trans. Antennas Propag.*, vol. 67, no. 2, pp. 853–860, Feb. 2019.

[15] G. Xu et al., "Microstrip grid and patch-based dual-band shared-aperture differentially fed array antenna," *IEEE Antennas Wireless Propag. Lett.*, vol. 20, no. 6, pp. 1043–1047, Jun. 2021.

[16] Y.-X. Sun and K. W. Leung, "Substrate-integrated two-port dual-frequency antenna," *IEEE Trans. Antennas Propag.*, vol. 64, no. 8, pp. 3692–3697, Aug. 2016.

[17] M. Ferrando-Rocher, J. I. Herranz-Herruzo, A. Valero-Nogueira, and B. Bernardo-Clemente, "Full-metal K-Ka dual-band shared-aperture array antenna fed by combined ridge-groove gap waveguide," *IEEE Antennas Wireless Propag. Lett.*, vol. 18, no. 7, pp. 1463–1467, Jul. 2019.

[18] T. Li and Z. N. Chen, "Wideband sidelobe-level reduced Ka-band metasurface antenna array fed by substrate-integrated gap waveguide using characteristic mode analysis," *IEEE Trans. Antennas Propag.*, vol. 68, no. 3, pp. 1356–1365, Mar. 2020.

[19] B. Feng, X. He, J. Cheng, and C. Sim, "Dual-wideband dual-polarized metasurface antenna array for the 5G millimeter wave communications based on characteristic mode theory," *IEEE Access*, vol. 8, pp. 21589–21601, 2020.

[20] W. Sun, Y. Li, L. Chang, H. Li, X. Qin, and H. Wang, "Dual-band dual-polarized microstrip antenna array using double-layer gridded patches for 5G millimeter-wave applications," *IEEE Trans. Antennas Propag.*, vol. 69, no. 10, pp. 6489–6499, Oct. 2021.

[21] H.-N. Hu, F.-P. Lai, and Y.-S. Chen, "Dual-band dual-polarized scalable antenna subarray for compact millimeter-wave 5G base stations," *IEEE Access*, vol. 8, pp. 129180–129192, 2020.

[22] Z. Siddiqui et al., "Dual-band dual-polarized planar antenna for 5G millimeter-wave antenna-in-package applications," *IEEE Trans. Antennas Propag.*, vol. 71, no. 4, pp. 2908–2921, Apr. 2023.

[23] Y. Zhang, W. Yang, Q. Xue, J. Huang, and W. Che, "Broadband dual-polarized differential-fed filtering antenna array for 5G millimeter-wave applications," *IEEE Trans. Antennas Propag.*, vol. 70, no. 3, pp. 1989–1998, Mar. 2022.

[24] J. Chen, M. Berg, K. Rasilainen, Z. Siddiqui, M. E. Leinonen, and A. Pärssinen, "Broadband cross-slotted patch antenna for 5G millimeter-wave applications based on characteristic mode analysis," *IEEE Trans. Antennas Propag.*, vol. 70, no. 12, pp. 11277–11292, Dec. 2022.

[25] Y. Li and K.-M. Luk, "60-GHz dual-polarized two-dimensional switch-beam wideband antenna array of aperture-coupled magneto-electric dipoles," *IEEE Trans. Antennas Propag.*, vol. 64, no. 2, pp. 554–563, Feb. 2016.

[26] X. Gu et al., "Development, implementation, and characterization of a 64-element dual-polarized phased-array antenna module for 28-GHz high-speed data communications," *IEEE Trans. Microw. Theory Techn.*, vol. 67, no. 7, pp. 2975–2984, Jul. 2019.

[27] C.-T. Chuang, T.-J. Lin, and S.-J. Chung, "A band-notched UWB monopole antenna with high notch-band-edge selectivity," *IEEE Trans. Antennas Propag.*, vol. 60, no. 10, pp. 4492–4499, Oct. 2012.

[28] H.-Y.-A. Yim and K.-K.-M. Cheng, "Novel dual-band planar resonator and admittance inverter for filter design and applications," in *IEEE MTT-S Int. Microw. Symp. Dig.*, Long Beach, CA, USA, Jun. 2005, pp. 2187–2190.

[29] J.-S. G. Hong, *Microstrip Filters for RF/Microwave Applications*. Hoboken, NJ, USA: Wiley, 2004.

[30] N.-W. Liu, L. Zhu, W.-W. Choi, and J.-D. Zhang, "A novel differential-fed patch antenna on stepped-impedance resonator with enhanced bandwidth under dual-resonance," *IEEE Trans. Antennas Propag.*, vol. 64, no. 11, pp. 4618–4625, Nov. 2016.

[31] B. Feng, J. Chen, K. L. Chung, L. Wang, and Y. Li, "Dual-polarized filtering magneto-electric dipole antenna arrays with high radiation-suppression index for 5G new radio n258 operations," *IEEE Trans. Antennas Propag.*, vol. 70, no. 4, pp. 3058–3063, Apr. 2022.

[32] K. Rasilainen, A. Lehtovuori, and V. Viikari, "LTE handset antenna with closely-located radiators, low-band MIMO, and high efficiency," in *Proc. 11th Eur. Conf. Antennas Propag. (EUCAP)*, Paris, France, Mar. 2017, pp. 3074–3078.